Structural Response of Phyllomanganates to Wet Aging and Aqueous Mn(II)

Margaret A. G. Hinkle*[†], Elaine D. Flynn, and Jeffrey G. Catalano

Department of Earth and Planetary Sciences, Washington University, 1 Brookings Drive, Saint Louis, MO 63130 USA

*Corresponding author: Tel.: +1-202-633-1815; E-mail: mhinkle@eps.wustl.edu

[†]Present address: Department of Mineral Sciences, Smithsonian Institution, National Museum of Natural History, Washington, DC 20560

Submitted to *Geochimica et Cosmochimica Acta*
May 2016
Revised July 2016

ABSTRACT

Naturally occurring Mn(IV/III) oxides are often formed through microbial Mn(II) oxidation, resulting in reactive phyllomanganates with varying Mn(IV), Mn(III), and vacancy contents. Residual aqueous Mn(II) may adsorb in the interlayer of phyllomanganates above vacancies in their octahedral sheets. The potential for interlayer Mn(II)-layer Mn(IV) comproportionation reactions and subsequent formation of structural Mn(III) suggests that aqueous Mn(II) may cause phyllomanganate structural changes that alters mineral reactivity or trace metal scavenging. Here we examine the effects of aging phyllomanganates with varying initial vacancy and Mn(III) content in the presence and absence of dissolved Mn(II) at pH 4 and 7. Three phyllomanganates were studied: two exhibiting turbostratic layer stacking (δ-MnO_2 with high vacancy content and hexagonal birnessite with both vacancies and Mn(III) substitutions) and one with rotationally ordered layer stacking (triclinic birnessite containing predominantly Mn(III) substitutions). Structural analyses suggest that during aging at pH 4, Mn(II) adsorbs above vacancies and promotes the formation of phyllomanganates with rotationally ordered sheets and mixed symmetries arranged into supercells, while structural Mn(III) undergoes disproportionation. These structural changes at pH 4 correlate with reduced Mn(II) uptake onto triclinic and hexagonal birnessite after 25 days relative to 48 hours of reaction, indicating that phyllomanganate reactivity decreases upon aging with Mn(II), or that recrystallization processes involving Mn(II) uptake occur over 25 days. At pH 7, Mn(II) adsorbs and causes limited structural effects, primarily increasing sheet stacking in δ-MnO_2. These results show that aging-induced structural changes in phyllomanganates are affected by aqueous Mn(II), pH, and initial solid-phase Mn(III) content. Such restructuring likely alters manganese oxide reactions with other constituents in environmental and geologic systems, particularly trace metals and redox-active compounds.

1. INTRODUCTION

Many naturally-occurring manganese oxides are nanoparticulate, poorly crystalline, and highly reactive minerals (Krumbein and Jens, 1981; Emerson et al., 1982; Villalobos et al., 2003; Saratovsky et al., 2006; Bargar et al., 2009; Clement et al., 2009; Dick et al., 2009; Grangeon et al., 2010; Tan et al., 2010). Manganese oxide formation in natural systems is often controlled by microbial Mn(II) oxidation, as abiotic Mn(II) oxidation is kinetically slow (Morgan and Stumm, 1964; Nealson et al., 1988; Tebo, 1991; Wehrli et al., 1995; Tebo et al., 1997; Von Langen et al., 1997; Bargar et al., 2000; Nelson and Lion, 2003; Morgan, 2005; Luther, 2010). Biogenic manganese oxides are typically phyllomanganates with birnessite-type structures, consisting of negatively charged octahedral sheets separated by hydrated interlayers (Krumbein and Jens, 1981; Emerson et al., 1982; Villalobos et al., 2003; Bargar et al., 2005; Webb et al., 2005a; Saratovsky et al., 2006; Bargar et al., 2009; Clement et al., 2009; Dick et al., 2009; Grangeon et al., 2010; Tan et al., 2010; Santelli et al., 2011). The negative layer charge develops as a result of Mn(IV) vacancies, Mn(III) substitutions, or a combination thereof, with vacancy and Mn(III) content varying substantially among phyllomanganates. To compensate the negative charge, exchangeable cations are adsorbed in the interlayer. These phyllomanganates exhibit high adsorption capacities for many cations, including Mn(II) (Morgan and Stumm, 1964; McKenzie, 1980; Murray et al., 1984), which often bind above vacant sites in the octahedral sheets (Toner et al., 2006; Peacock and Sherman, 2007; Manceau et al., 2007b; Peacock, 2009; Zhu et al., 2010b) and can enter into the phyllomanganate structure over time (Peacock, 2009).

Phyllomanganates coexist with aqueous Mn(II) in regions with active manganese cycling; for example, at hydrothermal vents, redox interfaces in soils or sediments, or in oxic regions of stratified soils, sediments, and water columns as a result of upward diffusion of Mn(II) (Graybeal

and Heath, 1984; Rajendran et al., 1992; Burdige, 1993; Van Cappellen et al., 1998; Tebo et al., 2004; Tebo et al., 2005). Abiotic reactions involving Mn(II) adsorption onto phyllomanganates are likely common in these environments (Shimmield and Price, 1986; Canfield et al., 1993), and could involve Mn(II) incorporation into vacant sites or electron transfer via Mn(II)-Mn(IV) comproportionation reactions, resulting in increased structural Mn(III). Several studies have identified that aqueous Mn(II) induces phyllomanganate phase transformations to a wide range of Mn(III) or Mn(IV/III) oxide minerals, including nsutite [$Mn(O,OH)_2$], ramsdellite [MnO_2], cryptomelane [$K_x(Mn^{IV},Mn^{III})_8O_{16}$], groutite [α-MnOOH] (Tu et al., 1994), hausmannite [Mn_3O_4] (Lefkowitz et al., 2013), feitknechtite [β-MnOOH] (Bargar et al., 2005; Elzinga, 2011; Lefkowitz et al., 2013; Elzinga and Kustka, 2015), or manganite [γ-MnOOH] (Tu et al., 1994; Elzinga, 2011; Lefkowitz et al., 2013; Elzinga and Kustka, 2015). A recent study has observed Mn isotope exchange between aqueous Mn(II) and a solid Mn(IV) oxide during conversion to Mn(III) oxyhydroxides, indicating that some Mn(III) formed during reaction undergoes disproportionation (Elzinga and Kustka, 2015).

Many natural systems with active manganese cycling are associated with Mn(IV/III) phyllomanganates, even in the presence of elevated dissolved Mn(II) (Wehrli et al., 1995; Friedl et al., 1997; Manceau et al., 2007a; Manceau et al., 2007b; Dick et al., 2009; Tan et al., 2010; Frierdich and Catalano, 2012), suggesting that Mn(II)-induced phase transformations of birnessite-type phyllomanganates are uncommon. Prior research on Mn(II)-phyllomanganate interactions with Mn(II) to Mn(IV) ratios that do not induce phase transformations is limited. Some studies do indicate that Mn(II) alters sheet stacking behaviors (Lefkowitz et al., 2013) and symmetries (Bargar et al., 2005; Zhu et al., 2010a; Zhao et al., 2016). This indicates that structural Mn(III) was produced during reaction, as its larger size and Jahn-Teller distortion are

111 expected to alter the mineral structure. However, the systematic relationship between Mn(II)
112 concentrations and phyllomanganate structural changes at low to circumneutral pH (conditions
113 relevant to soils and many natural waters) is unclear.

114 Identifying the structural response of phyllomanganates to dissolved Mn(II) is needed
115 because the reactivity and trace metal scavenging behavior of manganese oxides is largely
116 controlled by their structure (Post, 1999). In this paper, changes to phyllomanganate structures
117 are examined following aging for 25 days in the presence and absence of Mn(II) at acidic and
118 neutral pH, with Na^+ as the dominant cation. Because Mn(II) likely adsorbs above vacancies,
119 three birnessite-type phyllomanganates with varying vacancy content and layer stacking are
120 investigated. δ-MnO_2, the synthetic analogue of vernadite [$(Ca,Na,K)(Mn^{4+},\square)O_2 \bullet nH_2O$]
121 (Villalobos et al., 2006), has high vacancy content and turbostratic stacking; c-disordered H^+
122 birnessite (a hexagonal-type birnessite) ('HexB') [$(Ca,Na,K)(Mn^{4+},Mn^{3+},\square)O_2 \bullet nH_2O$] has
123 vacancies (Silvester et al., 1997; Lanson et al., 2000), Mn(III) substitutions, and turbostratic
124 stacking; triclinic birnessite ('TriB') [$(Ca,Na,K)(Mn^{4+}_{x}Mn^{3+}_{1-x})O_2 \bullet nH_2O$] has primarily Mn(III)
125 substitutions, few vacancies, and ordered layer stacking (Post and Veblen, 1990; Drits et al.,
126 1997; Post et al., 2002; Lopano et al., 2007). The role of pH is also examined because
127 Mn(II)-Mn(IV) comproportionation reactions exhibit a pH dependence, with comproportionation
128 promoted with increasing pH (Mandernack et al., 1995). The effects of aging and Mn(II) on
129 phyllomanganate sheet structures were explored using X-ray absorption fine structure (XAFS)
130 spectroscopy and powder X-ray diffraction (XRD). To assess differences in Mn(II) uptake upon
131 aging versus adsorption over short time scales, macroscopic Mn(II) adsorption isotherms onto
132 the solids at differing pH values were also obtained.
133

2. METHODS AND MATERIALS

2.1 Mn Oxide Syntheses

Manganese oxide minerals were synthesized using modified, previously published procedures, as described in detail below. δ-MnO_2 was synthesized using a redox method, which involves the reduction of $KMnO_4$ and the oxidation of $MnCl_2$ under alkaline conditions, outlined by Villalobos et al. (2003). Briefly, a solution of 2.50 g $KMnO_4$ in 80 mL deionized water (>18.2 MΩ·cm) was added to a solution of 1.75 g NaOH in 90 mL deionized water over approximately five minutes. While stirring this mixture vigorously, a solution of 4.70 g $MnCl_2$•$4H_2O$ in 80 mL deionized water was added slowly, over approximately 35 minutes. The mixture was allowed to settle for four hours, after which point the pH of the suspension was checked to ensure it was around a pH of 7, and the suspension was centrifuged, discarding the supernatant. The suspension was subjected to at least four 1 M NaCl washes, as described in Villalobos et al. (2003), followed by at least six deionized water washes.

A poorly crystalline hexagonal birnessite was synthesized following the c-disordered H^+-birnessite synthesis procedure described in Villalobos et al. (2003). This synthesis is similar to the δ-MnO_2 synthesis described above (including the NaCl and deionized water washes), except the NaOH solution consisted of 1.83 g NaOH in 90 mL deionized water, the Mn(II) solution consisted of 5.82 g $MnCl_2$•$4H_2O$ in 80 mL deionized water, and the pH of the suspension prior to centrifugation was near 3.1. Triclinic birnessite was prepared following the synthesis for Na-birnessite outlined in Lopano et al. (2007), based on the synthesis procedures described by Post and Veblen (Post and Veblen, 1990) and Golden et al. (1986; 1987). In this synthesis, a 5.5 M NaOH solution and a 0.5 M $MnCl_2$•$4H_2O$ solution were chilled in an ice bath while air was vigorously bubbled through the Mn(II) solution. Once the solutions were chilled to

157 5ºC, the NaOH solution was added to the Mn(II) solution over approximately 3 minutes under a
158 fume hood. The resulting suspension was bubbled with air overnight in the fume hood. The
159 suspension was washed by an initial centrifugation to remove the basic supernatant, followed by
160 filtration (0.45 μm nylon membrane, Whatman®) and washing with deionized water until the pH
161 of the filtrate was below 10.
162 After synthesis, the minerals were resuspended in DI water, transferred to an anaerobic
163 chamber (Coy Laboratory Products, Inc., 3% H_2/97% N_2 atmosphere with Pd catalysts) and
164 sparged for at least 24 hours with a gas filtration system (Hinkle et al., 2015) to remove
165 dissolved O_2 from the suspensions. The minerals were stored within the anaerobic chamber as
166 suspensions in deionized water in aluminum foil-wrapped polypropylene bottles and were used
167 for experiments within the month. Aliquots of the mineral suspensions were dried at 70 ºC for
168 surface area analysis by BET N_2 gas adsorption (Quantachrome Instruments Autosorb-1).
169
170 **2.2 Reagent preparation**
171 All stock solutions for experiments conducted in this study were prepared in the
172 anaerobic chamber using deoxygenated deionized water. The Mn(II) stock solution was prepared
173 from $MnCl_2$•$4H_2O$ and stored in an amber polypropylene bottle to prevent photo-oxidation. NaCl
174 and 2-(4-morpholino)ethanesulfonic acid (MES) stock solutions were also prepared. For
175 experiments conducted at pH 7, a stock solution comprised of both NaCl and MES was prepared
176 and adjusted to pH 7 using HCl or NaOH solutions, which were sparged using the gas filtration
177 systems more than six months prior to use. The HCl and NaOH solutions were also used to
178 adjust experiment sample pH.
179

2.3 Solid Mn(IV/III) Oxide Aging Experiments

The effect of Mn(II) on phyllomanganate sheet structures was explored by collecting XAFS spectra and XRD patterns on phyllomanganates reacted with varying concentrations of Mn(II). In these experiments, 10 mM NaCl (required to buffer ionic strength) and 0, 0.75, or 7.5 mM Mn(II) were reacted with 2.5 g L^{-1} δ-MnO_2, HexB, or TriB at pH 4 or 7 for 25 days in an anaerobic chamber (Coy Laboratory Products, Inc., 3% H_2/97% N_2 atmosphere with Pd catalysts). 1 mM MES pH buffer was used for TriB pH 7 experiments as well as preliminary pH 7 δ-MnO_2 and HexB experiments.

For samples reacted with Mn(II), the ratio of initial aqueous Mn(II) to solid Mn(IV) (mol:mol) in these experiments range from 0.042-0.543 (Table 1). Samples were prepared in 15 mL or 50 mL conical centrifuge tubes for the XAFS and XRD analyses, respectively. The pH of the samples were monitored throughout the experiments. At the end of 25 days, the final pH of each sample was recorded and the samples were filtered (reusable syringe filter; 0.22 μm MCE membrane; Fisher Scientific) to collecting the solids and supernatant fluid for analyses; the first 1 mL of supernatant was discarded. The fluid was acidified to 2% HNO_3 (trace metal grade; Fisher Scientific) immediately after removal from the anaerobic chamber. Aliquots of the acidified fluid were diluted using 2% HNO_3 and analyzed for total Mn concentration by inductively-coupled plasma optical emission spectroscopy (ICP-OES) using a Perkin Elmer Optima 7300 DV instrument. Sample uncertainty (95% confidence level) was calculated for these samples by the triplicate instrument analyses.

2.4 XRD Analyses

For XRD analyses, the samples were dried at ambient temperature (22±1°C) in a vacuum

desiccator, then ground with an agate mortar and pestle and stored within glass vials, all within the anaerobic chamber. XRD slides were prepared in the anaerobic chamber and sealed with an airtight dome to maintain anoxic conditions. However, use of the dome substantially attenuated the X-ray beam intensity, decreasing the signal to noise ratio, and produced large background scattering features at 9 to 18° and above 65° 2θ. XRD patterns were collected for all samples reacted with 7.5 mM Mn(II) with and without the dome to test the stability of these materials in air during analysis (approximately 40 minutes). No changes were observed between patterns collected with and without the dome for these high Mn(II) experiments, consistent with the known slow kinetics of Mn(II) oxidation by O_2 (Morgan, 2005; Luther, 2010). All other samples were thus assumed to be air-stable for the duration of the XRD analyses and were measured only in air; all XRD presented here were collected without the dome. To minimize air exposure, these were transferred to the XRD instrument within the airtight dome, which was removed immediately prior to data collection. Unreacted phyllomanganates were dried immediately after synthesis and were prepared and analyzed following the same methods for the aged samples, but in air rather than under anaerobic conditions. XRD patterns were collected from 5-80° 2θ with 0.04° 2θ steps at 3 seconds $step^{-1}$ with Cu K_α radiation, a LynxEyeXE Si strip detector, a 0.6 mm anti-scatter slit, and a 2.5° incident soller slit, with the X-ray tube voltage and current set to 40 kV and 40 mA, respectively.

2.5 XAFS Spectroscopy

2.5.1 XAFS Data Collection

Samples prepared for XAFS spectroscopic analyses were packed as wet pastes on a syringe filter membrane enclosed in Kapton film and sealed with 25 μm Kapton tape within the

anaerobic chamber. Each XAFS sample was heat sealed in a polyethylene bag with a damp KimWipe to maintain anoxic and hydrated conditions during transport to the Advanced Photon Source (APS) at Argonne National Laboratory. Hydrated conditions were further ensured by filtering and preparing the solids within 48 hours of transport to the APS. Wet pastes of synthesized, unreacted δ-MnO_2, HexB, and TriB were also filtered and prepared for XAFS spectroscopic measurements as described above. XANES spectra of synthetic bixbytite [Mn_2O_3], rhodochrosite [$MnCO_3$], and 1 M $MnSO_{4(aq)}$ were also collected. The minerals were prepared for XAFS spectroscopy by grinding with an agate mortar and pestle for approximately 15 minutes and spreading the resulting fine powder on Scotch tape. The 1 M $MnSO_4$ solution was prepared for XAFS measurements by sealing the solution in a polycarbonate sample holder with Kapton tape.

XAFS spectra were collected in transmission at beamlines 5-BM-D and 12-BM-B at the Advanced Photon Source (APS) at Argonne National Laboratory. 5-BM-D uses a Si (111) fixed-offset double-crystal monochromator, which was detuned by 40% to decrease harmonics in the incident X-ray beam. Rh-coated Si mirrors optimize the beam height and further reduce the harmonic content. 12-BM-B also uses a Si (111) fixed-offset double-crystal monochromator, which was detuned by 20%, and has toroidal focusing and flat harmonic rejection mirrors. XAFS spectra of a Mn metal foil, collected simultaneously with each sample scan, was used to calibrate the monochromators to the Mn K-edge (6539 eV).

2.5.2 XAFS Spectral Fitting

The XAFS spectra were averaged, processed, and normalized using the Athena (Ravel and Newville, 2005) interface to IFEFFIT (Newville, 2001). The average manganese oxidation

249 state (AMOS) for each sample was calculated using linear combination fitting (LCF) of the
250 normalized XANES spectra in Athena with the following manganese oxidation state standards:
251 $MnCO_3$, 1 M $MnSO_{4(aq)}$, bixbyite, feitknechtite, and three Mn(IV) standards in the database
252 provided in Manceau et al. (2012): KBi (a K^+-birnessite), ramsdellite, and pyrolusite (Figure
253 EA1). These fits followed a modified approach described Manceau et al. (2012), in which six or
254 fewer reference oxidation state standards with non-negative loadings are fit to a sample using
255 LCF. The accuracy of these manganese oxidation valence state fits are difficult to calculate
256 through traditional methods, but are estimated to be ±0.04 v.u., with decreasing accuracy with
257 increasing $Mn^{3+/2+}$ content (Manceau et al., 2012).
258 Fitting of the k^3-weighted EXAFS spectra was conducted in SixPack (Webb, 2005) using
259 a structural model similar to that described in detail by Webb et al. (2005a). A Na-birnessite
260 (phyllomanganate) structure (Post and Veblen, 1990) was used to calculate backscattering phase
261 and amplitude functions using FEFF 7 (Ankoudinov, 1996). The EXAFS spectra were fit over a
262 k range of 3 – 15.3 $Å^{-1}$ and an R range of 1 – 6 Å. The amplitude reduction factor (S_0^2) was fixed
263 to 0.835 following Webb et al. (2005a). The model employed three Mn-O shells and three
264 Mn-Mn shells, with each shell including two paths to account for potential Jahn-Teller distorted
265 Mn(III)-induced warping of the phyllomanganate sheet. Corner-sharing Mn-Mn (likely Mn
266 bound above sheet vacancies) and interlayer Mn-Na were also included in the model. All five
267 possible Mn-Mn multiple scattering (MS) paths for the third Mn-Mn shell were included in the
268 model, but only contributed 1 additional fitting variable (σ^2) to the fit as their coordination
269 numbers and distances could be constrained fully using the constituent single scattering (SS)
270 paths. The σ^2 values between linked paths were fixed, and second and third shell Mn-Mn
271 distances were fixed based on the geometrical constrains defined by the first Mn-Mn shell. Every

Mn-Mn scattering path included a parameter to account for vacancy effects on the amplitude, f_{occ}: the fraction of Mn sites occupied in the phyllomanganate sheet. It should be noted that this f_{occ} parameter correlates strongly with particle size (Webb et al., 2005a). Attempts to include the β parameter from the Webb et al. (2005a) model to improve fitting a weak feature in the Fourier transform spectra at ~5.2 Å (R+ΔR) generally yielded no effect on other structural parameters (e.g., f_{occ} or Mn path splitting). β did not vary systematically among the samples and often had large uncertainties, with values within error of zero. As the feature at ~5.2 Å was adequately fit (Figure EA2) by allowing a Mn-Mn MS σ^2 parameter to vary, the β parameter was not included in the final model.

2.6 Macroscopic Mn(II) Adsorption Experiments

Mn(II) adsorption isotherms were measured after 2 days of reaction for each phyllomanganate mineral to assess Mn(II) uptake on short time scales compared to results observed in the aging studies described above. All experiments were conducted within the anaerobic chamber with 10 mM NaCl (to buffer ionic strength), 2.5 g L^{-1} phyllomanganate, and 0.02 – 12 mM aqueous Mn(II) at pH 4, wrapped in aluminum foil and rotated on end-over-end rotators for two days. pH 7 studies were not conducted because no dissolved Mn(II) was detected at the end of the aging studies, preventing comparison to short time scale adsorption isotherms. Samples at 0.10 mM Mn(II) were prepared in triplicate and as mineral-free blanks to assess systematic experimental errors. Samples were allowed to equilibrate for approximately an hour, at which point the pH of each sample was adjusted using HCl or NaOH. The sample pH was checked and adjusted if necessary throughout the reaction period.

At the end of the experiments, the pH of the samples was recorded and the samples were

295 filtered (0.22 μm MCE filters; Fisher Scientific). The pH of all samples drifted by less than 0.1
296 pH units, except under high Mn(II) conditions [i.e., > 9 mM initial Mn(II)] with the TriB system,
297 which all had final pH drifts greater than 0.5 pH units from the target pH. Due to the large pH
298 drifts in the TriB samples with > 9 mM initial Mn(II), these samples were discarded from the
299 final reported isotherm. The filtrate was collected after discarding the first 1 mL of filtrate and
300 prepared for ICP-OES measurements as described above. Both the triplicate instrument analyses
301 and the standard deviations from the triplicate experiment samples (propagated to the entire
302 sample set) were used to calculate experimental uncertainty at 95% confidence level. The
303 adsorption data was fitted to Langmuir isotherms (Table EA1) to facilitate quantitative
304 comparison to Mn(II) uptake after aging.
305
306 **3. RESULTS**
307 **3.1 Synthesized Materials**
308 The three phyllomanganates used in this work, δ-MnO_2, HexB, and TriB, exhibit
309 properties consistent with past studies (Villalobos et al., 2003; Webb et al., 2005a). HexB (167.8
310 $m^2\ g^{-1}$) and δ-MnO_2 (116.4 $m^2\ g^{-1}$) have much larger BET-derived surface areas than TriB (24.8
311 $m^2\ g^{-1}$), and the Mn(III) content decreases from TriB to HexB to δ-MnO_2 (Table EA2). The XRD
312 patterns of δ-MnO_2 and HexB (Figure 1A) exhibit broad, low-intensity (001) and (002) peaks
313 near 12.3 and 24.8° 2θ, respectively, indicating that few sheets are stacked along the *c*-axis [i.e.,
314 ~1-4 sheets (Lanson et al., 2008; Grangeon et al., 2010; Grangeon et al., 2012)]. The δ-MnO_2
315 and HexB XRD patterns also contain asymmetric (20,11) and (02,31) bands near 37 and 65° 2θ,
316 respectively, characteristic of turbostratic phyllomanganates (Villalobos et al., 2003; Webb et al.,
317 2005a; Webb et al., 2005b), with d-spacing ratios consistent with hexagonal sheet symmetry

(i.e., d-spacing ratio of (20,11)/(02,31) ~√3) (Villalobos et al., 2003; Villalobos et al., 2006; Grangeon et al., 2010). The HexB XRD pattern also exhibits a decrease in intensity near 46° 2θ relative to the (20,11) band maxima at 38°, indicating vacancies in the sheet are capped by Mn or other cations (Villalobos et al., 2006; Grangeon et al., 2010; Grangeon et al., 2012). In contrast, the TriB XRD pattern (Figure 1A) is consistent with rotationally ordered sheets with pseudo-orthogonal symmetry and a large coherent scattering domain along the *c*-axis (Brindley and Brown, 1980).

The EXAFS spectra (Figure 2) also indicate that δ-MnO_2 and HexB have hexagonal sheet symmetry while TriB is pseudo-orthogonal. Prior work has shown that the positive antinodes at ~6.8, ~8.1, and 9.2 $Å^{-1}$ shift to lower k values, with the latter two splitting, when phyllomanganate sheets transition from hexagonal to pseudo-orthogonal symmetry (Marcus et al., 2004; Manceau et al., 2005; Webb et al., 2005a; Zhu et al., 2010a; Yu et al., 2012). The positive antinode at ~6.8 $Å^{-1}$ is considered characteristic of layered manganese oxides (McKeown and Post, 2001). These differences in sheet symmetry are manifested in the Fourier transform spectra, with the Mn MS peak at 5.2 Å (R+ΔR) becoming attenuated from sheet bending arising from Jahn-Teller distorted Mn(III) substitution (Webb et al., 2005a; Bargar et al., 2009).

The EXAFS spectra are also sensitive to the presence of Mn atoms capping vacancy sites, although quantification of the abundance of such species by this method is poor (Webb et al., 2005a). The dominant oxidation state of capping Mn atoms can be estimated by combining the distance between these atoms and Mn atoms in the phyllomanganate sheet (the Mn-Mn_{crnr} path in the structural fitting model; Table EA3), the AMOS (Table 2), and fine-structure features in the XANES spectrum, specifically a shoulder at ~6553 eV that indicates the presence of sorbed

Mn(II) (Bargar et al., 2000; Villalobos et al., 2003; Webb et al., 2005a). The Mn-Mn_{crnr} distance (Table EA3) is shorter in TriB (3.36 Å) than in HexB (3.45 Å). The distance in TriB is consistent with Mn(III), as Jahn-Teller distortion yields shorter corner-sharing Mn-Mn distances for this oxidation state than for a Mn(II) neighbor (Post et al., 1982). For δ-MnO_2 the AMOS of 3.99 (Table 2), lack of a shoulder at 6553 eV, no distinct feature at 3.0 Å (R+ΔR) in the Fourier transform (corresponding to the Mn-Mn_{crnr} shell), and better EXAFS spectral fit when excluding Mn-Mn_{crnr} from the model (Figure EA2) all indicate that few vacancy-capping Mn atoms are present in unreacted δ-MnO_2. The Mn(II) content of the HexB material (Table EA2) and the longer Mn-Mn_{crnr} distance suggest that interlayer Mn over vacancies is predominately Mn(II).

3.2 Effect of Aging and Mn(II) on Turbostratic Phyllomanganates

pH 4

δ-MnO_2 and HexB sheet structures change substantially after 25 days of aging at pH 4 in both the absence and presence of aqueous Mn(II). XANES spectra (Figure 2) indicate that AMOS decreases with increasing initial aqueous Mn(II) (Table 2), and the Fourier transforms of the EXAFS spectra (Figure 2) suggest increased Mn-Mn_{crnr} contributions, both consistent with Mn(II) sorption onto the phyllomanganates during the 25 day reaction. While Mn(II) uptake onto δ-MnO_2 after aging closely matched uptake behavior observed on short time scales, adsorption by HexB decreased upon aging (Figure 3). This suggests that structural properties of the phyllomanganates change during aging.

The XRD patterns of δ-MnO_2 reacted with 0 and 0.75 mM Mn(II) at pH 4 (Figure 1) exhibit a minimum near 46° 2θ compared to the unaged sample, consistent with Mn adsorption over vacancies (Villalobos et al., 2006; Grangeon et al., 2010; Grangeon et al., 2012). The

decrease in f_{occ} (Table EA4) and AMOS of 3.99 (Table 2) for the 0 mM Mn(II) sample suggests that either Mn migrates out of the phyllomanganate sheet and into vacancy-capping sites or that the phyllomanganate crystallite size simply decreases during aging, although the latter scenario should be accompanied by an increase in the width of the *hk0* bands in XRD, which is not observed (Figure 1). The small Mn-Mn_{crnr} contribution in the EXAFS model fit and its distance of 3.28 Å further indicate that some layer Mn(III/IV) is redistributed to the interlayer to adsorb over vacancies upon δ-MnO_2 aging at pH 4. For the 0.75 mM Mn(II) sample, however, the AMOS and presence of a shoulder at 6553 eV in the XANES spectrum indicate the addition of sorbed Mn(II).

The XRD patterns of the 7.5 mM Mn(II) δ-MnO_2 sample and all aged HexB samples exhibit substantial changes compared to the unreacted sample, with the (11,20) and (31,02) bands splitting and the appearance of additional peaks in the 20-70° 2θ region (Figure 1B,C). These additional peaks do not correspond with the diffraction lines of known manganese oxides, including tectomanganates like todorokite or cryptomelane (Table EA5). The additional XRD peaks are thus not from the formation of a secondary manganese mineral. Similar peaks between ~35-70° 2θ have been previously observed for an H-exchanged hexagonal birnessite ('HBi') formed by equilibration of triclinic Na-buserite at pH 5 (Lanson et al., 2000) and for HBi with Zn adsorbed over vacancies (Lanson et al., 2002; Drits et al., 2007). These were interpreted as containing an interstratified defective layer structure (Lanson et al., 2000; Lanson et al., 2002; Drits et al., 2007), as the *hkl* peak positions in such cases lie between the *hkl* positions of each of the layer-types present in the material (Drits and McCarty, 1996). These materials were best described by models consisting of interspersed hexagonal and orthogonal sheets with rotated stacking behaviors and each sheet displaced along the a axis by +a/3 (Lanson et al., 2000;

Lanson et al., 2002), analogous to the chalcophanite structure (Post and Appleman, 1988). This structure minimizes electrostatic repulsion, maximizing the distance between Mn atoms in adjacent sheets and the distance between sheet Mn sites and Mn atoms capping vacancies (Lanson et al., 2000; Lanson et al., 2002). Analogous XRD patterns have been reported for rotationally ordered Ca-montmorillonite, with (11,20) and (31,02) band splitting and relative intensities similar to those observed in this paper (Viani et al., 2002).

This structural arrangement was further shown to produce supercell ordering in phyllomanganates (Drits et al., 2002). XRD features in the 20-26^{o} 2θ region not associated with the (002) reflection in the present study are consistent with supercell peaks previously observed for this class of minerals (Drits et al., 1998). All of the samples with these XRD features have weak layer stacking so the long range ordering responsible for the supercell must be located in the *a-b* plane. These results thus indicate that the phyllomanganate sheet structure formed after δ-MnO_2 reacts with 7.5 mM Mn(II) or when HexB is aged with or without added dissolved Mn(II) is likely a mixture of hexagonal and pseudo-orthogonal phyllomanganate sheets that are rotationally ordered in their stacking and contain long-range sheet-parallel periodicity. These aging-induced HexB structural changes may explain the observed reduction in Mn(II) uptake by HexB but not δ-MnO_2 upon aging relative to uptake over short time scales (Figure 3). The initiation of this ordering transition in HexB under all aging conditions yet only at the highest Mn(II) loading for δ-MnO_2 suggests that a threshold Mn(III) content may exist, below which rotational ordering and supercell formation do not occur upon aging. Valence state measurements (Table 2) suggest that an AMOS less than ~3.8 is required to induce this restructuring; in the samples studied, this corresponds to 10-15 mol.% Mn(III).

The EXAFS spectra of δ-MnO_2 and HexB further confirm that the XRD features do not

arise from a phase transformation but instead from changes in sheet symmetry and ordering, as the primary phyllomanganate structure (i.e., MnO_6 octahedra arranged in negatively charged sheets) is preserved during aging and reaction with Mn(II) (Figure 2). Both HexB and δ-MnO_2 reacted with 0.75 mM Mn(II) exhibit minimal changes relative to the samples aged without added Mn(II). δ-MnO_2 reacted with 7.5 mM Mn(II), however, shows dampening and slight broadening of the 6.8 and 9.2 $Å^{-1}$ features in the EXAFS spectrum, which could be attributed to the formation of a phyllomanganate with mixed sheet symmetries. All δ-MnO_2 and HexB samples that show evidence of mixed sheet symmetries and supercell ordering display either an increase in splitting of the Mn-O_1 interatomic distances in the structural fitting model or a reduction in splitting in this shell coupled with a large σ^2 value for the more distant Mn-O_{1b} shell (Table EA4). We attribute these effects to the formation of a mixture of sheets with slightly different structures that corresponds to the larger-scale structural changes identified by XRD. No other systematic changes were apparent, indicating preservation of the overall phyllomanganate sheet during aging and reaction with Mn(II) at pH 4.

pH 7

δ-MnO_2 and HexB aged at pH 7 exhibit behavior considerably different than when reacted at pH 4. No substantial restructuring or formation of supercell ordering is observed at higher pH, with or without Mn(II) addition (Figure 1B,C). δ-MnO_2 shows sharper (001) and (002) peaks after aging with 0.75 mM Mn(II) present (Figure 1B), indicating that more sheets are stacked along the *c*-axis. For HexB aged with and without 0.75 mM Mn(II), the XRD patterns (Figure 1C), EXAFS spectra (Figure 2) and structural fitting parameters (Table EA4) at pH 7 are largely unchanged during aging and reaction with Mn(II), indicating little alteration of the

433 phyllomanganate sheet structure occurs. Reduction of the AMOS (Table 2) and a decrease near
434 46° 2θ in the XRD pattern (Figure 1) (Villalobos et al., 2006; Grangeon et al., 2010; Grangeon et
435 al., 2012) indicate that Mn(II)-HexB interactions are primarily limited to Mn(II) adsorption
436 reactions at pH 7. However, for both δ-MnO_2 and HexB, structural changes and a decrease in
437 AMOS were observed at this pH in the presence of MES buffer (see Electronic Annex). All
438 samples reacted with higher Mn(II) concentrations, 7.5 mM, at pH 7 exhibit substantial
439 feitknechtite precipitation as demonstrated by the corresponding XRD patterns (Figure 4A),
440 resulting in substantial changes in the XANES spectra (Figure 4B) and making it impossible to
441 assess how the structure of the residual phyllomanganate responds.
442
443 **3.3 Effect of Aging and Mn(II) on TriB**
444 *pH 4*
445 Like δ-MnO_2 and HexB, TriB also undergoes structural changes when aged at pH 4 in the
446 absence and presence of aqueous Mn(II), although the changes to the TriB structure are distinct
447 from those displayed by the turbostratic phyllomanganates. The XRD patterns show that aging
448 TriB at this pH with or without added Mn(II) results in a hexagonally symmetric material with
449 weaker rotational ordering of layers than the unreacted sample (Figure 1D). The d-spacing ratio
450 between reflections in all TriB samples are ~1.73, in agreement with a hexagonal unit cell
451 (Villalobos et al., 2003; Villalobos et al., 2006; Grangeon et al., 2010). The EXAFS spectra
452 clearly show that TriB reacted at pH 4 no longer possesses pseudo-orthogonal sheet symmetry,
453 as the maxima centered at 6.8, 8.1, and 9.2 $Å^{-1}$ in hexagonally symmetric phyllomanganates are
454 no longer shifted to lower k values as in unreacted TriB, and each is a single positive antinode.
455 Structural fitting of the spectra (Figure EA2) reveal that Mn-Mn_{crnr} distances increased

456 from 3.36 Å in unreacted TriB to 3.49 Å in TriB aged in the absence and presence of Mn(II).
457 This change in Mn-Mn_{crnr} distances, in conjunction with the appearance of a shoulder at ~6553
458 eV and the white line shift toward higher energy in the XANES spectra (Figure 2G) (Bargar et
459 al., 2000; Villalobos et al., 2003; Webb et al., 2005a), indicate that Mn atoms capping vacancies
460 shift from predominately Mn(III) to Mn(II), and that this is coupled with an increase in structural
461 Mn(IV) content. Fitting of the XANES spectra reveal a decreasing Mn(III) content coupled with
462 increasing Mn(II) and Mn(IV) contents upon aging TriB at pH 4 (Table EA2). Furthermore, the
463 amount of Mn(II) remaining in solution at the end of the 0 mM and 0.75 mM Mn(II) 25 day
464 experiments is greater than the initial amount of Mn(II) added to the systems (Table 2),
465 indicating that Mn(II) is released to solution via disproportionation of structural Mn(III). In
466 contrast, Mn(II) uptake by TriB after 48 hours follows typical Langmuir isotherm adsorption
467 behavior (Figure 3), with no net Mn(II) release observed, demonstrating the role of aging in
468 altering the structure and reactivity of TriB. These observations are consistent with TriB
469 transitioning to a phyllomanganate with hexagonal symmetry as a result of aging for 25 days
470 under low pH conditions that favor Mn(III) disproportionation.
471 TriB samples reacted with differing amounts of aqueous Mn(II) show minor systematic
472 changes in the XRD patterns and EXAFS spectra. The Fourier transforms of the EXAFS spectra
473 (Figure 2I) show a slight shift in the first Mn-Mn shell position in the presence of 7.5 mM
474 Mn(II), as well as an increased intensity of the ~3.0 Å feature corresponding to the Mn-Mn_{crnr}
475 shell. Increasing aqueous Mn(II) shifts the XRD (001) and (002) peak positions to higher 2θ
476 values (Figure EA3) with the (001) d-spacing, which corresponds to the interlayer spacing
477 between phyllomanganate sheets, decreasing by 0.03-0.05 Å. Additionally, XRD peaks in the
478 35-70^{o} 2θ region shift systematically with Mn(II) addition (Figure EA3). This indicates that the

addition of Mn(II) alters the sheet stacking or interlayer displacement, as has been invoked to explain similar XRD peak shifts in past studies (Lanson et al., 2002; Drits et al., 2007). The addition of 0.75 and 7.5 mM Mn(II) also leads to changes in low intensity XRD peaks at ~22° 2θ and in the 30-34° 2θ region by shifting their positions and increasing their intensities, respectively (Figure EA3). These peaks at ~22° 2θ and in the 30-34° 2θ region are consistent with the supercell reflections discussed above. These observations further support the conclusion that the addition of Mn(II) alters phyllomanganate long range ordering.

pH 7

XRD patterns show that the TriB sheet structure is much more stable at pH 7 than at pH 4, with little difference between the unreacted TriB and the sample aged in the absence of Mn(II) (Figure 1). The EXAFS spectra, however, suggest that some aging-induced restructuring occurs as the antinode at 8.1 $Å^{-1}$ is no longer split and shifted, as in unreacted TriB, although the positive antinodes near at 6.8 and 9.2 $Å^{-1}$ are unchanged (Figure 2H). Structural fitting of the spectrum (Figure EA2) suggests that these changes may be the result of increased splitting in the first Mn-Mn shell and a lengthening of Mn-Mn_{crnr} (Table EA4). These results indicate that the coordination environments of some Mn octahedra in the phyllomanganate sheet change and that a portion of the capping atoms over vacancies are altered from Mn(III) to Mn(II). The AMOS results are within error of the unreacted material, but the fraction of Mn(III) decreases while the fractions of Mn(IV) and Mn(II) slightly increase (Table EA2) suggesting that some Mn(III) may disproportionate, leading to more vacancy capping Mn(II) as indicated by the structural EXAFS fits. These AMOS values also show that no redox interactions occurred between TriB and the MES buffer, as those derived by XANES LCF are in agreement with those calculated by mass

balance (Table 2).

The EXAFS spectrum of TriB aged in the presence of 0.75 mM Mn(II) shows additional changes to the 6.8 and 9.2 $Å^{-1}$ positive antinode (Figure 2H). These antinodes are still much broader than those in the pH 4 system, but are consistent with a transition toward hexagonal symmetry. A reduction in the splitting of the first Mn-O shell occurs, and the Mn-Mn_{crnr} shell increases substantially in coordination number, suggesting an increase of capping atoms over vacancies (Table EA4). However, the minor feitknechtite component (Figure 1D), which consists of a hexagonal Mn(III)-bearing sheet (Meldau et al., 1973), may cause destructive interference in the EXAFS spectrum and it is thus uncertain whether the observed spectral changes correspond to real structural alteration or are an artifact.

4. DISCUSSION

4.1 Mechanism of Mn(II)-Induced Phyllomanganate Structural Changes

These results indicate that in addition to adsorption, dissolved Mn(II)-phyllomanganate interactions result in structural changes, which involve altered sheet symmetries and long-range order within the sheet itself. The extent of these Mn(II)-induced structural alterations appear to be dependent on both initial structural Mn(III) content and the pH of the solution. At pH 4 in the absence of Mn(II), some structural Mn is ejected from turbostratic phyllomanganate sheets, which then adsorbs above vacancies. The addition of aqueous Mn(II), which also adsorbs above vacancy sites, promotes the formation of a phyllomanganate with mixed sheet symmetries in the δ-MnO_2 and HexB systems. In these cases, pseudo-orthogonal and hexagonal layers are intermixed and the sheets are rotationally ordered to minimize repulsion between high valence Mn in adjacent layers and Mn in the interlayer (Lanson et al., 2002). These changes also occur

upon aging HexB at pH 4 in the absence of Mn(II), concurrent with ejection of some structural Mn. Increasing Mn(II/III) adsorption over vacancies may enhance electrostatic repulsion with layer Mn(IV) in adjacent sheets, which would promote rotationally ordered stacking. In addition, Mn(II) adsorption followed by comproportionation forms Mn(III) in the phyllomanganate sheet, promoting a change from hexagonal to pseudo-orthogonal layer symmetry. These effects of Mn(II) addition appear to promote long range ordering in the plane of the phyllomanganate sheets, forming a supercell. Sheet-parallel ordering of vacancy sites capped by adsorbed Mn at repeat distances greater than the unit cell size or ordering of pseudo-orthogonal and hexagonal domains within the sheets could generate the observed supercell. Sheet restructuring only occurs in samples with AMOS < ~3.8 containing 10-15 mol.% Mn(III), suggesting that a threshold Mn(III) content is required to induce the observed structural changes. This hypothesized Mn(III) threshold may originate because changes in sheet symmetry and ordering of vacancy capping atoms likely increases with increasing Mn(III) content.

The distinct behavior of TriB at pH 4 results from extensive Mn(III) disproportionation dominating over other processes. This disproportionation relaxes Jahn-Teller-induced sheet strain and leads to the formation of a hexagonally-symmetric material. The hexagonal sheet symmetry at pH 4 is still observed with the addition of Mn(II). These results indicate that the amount of Mn(II) added is inadequate to promote Mn(II)-Mn(IV) comproportionation, which favors orthogonal sheet symmetry, over disproportionation.

Structural changes are much more muted at pH 7 following aging in the absence and presence of Mn(II). δ-MnO_2 sheet stacking increases upon addition of Mn(II), while in the HexB system, aqueous Mn(II) does not appear to alter the manganese oxide structure, restricting its interaction to adsorption over vacant sites. TriB showed minor changes in the phyllomanganate

548 sheet and far less disproportionation than at pH 4, with Mn(III) being more stable at this pH
549 (Mandernack et al., 1995). We hypothesize that phyllomanganates with larger numbers of
550 vacancies (i.e., δ-MnO_2) may exhibit greater structural changes (barring phase transformations)
551 upon addition of aqueous Mn(II) at pH 7 as these are the sites where Mn(II) reacts with the
552 mineral phase. Feitknechtite precipitation at higher Mn(II) loadings is consistent with substantial
553 prior research on such phase transformations, which likely involve pH-dependent Mn(II)-Mn(IV)
554 comproportionation reactions (Elzinga, 2011; Lefkowitz et al., 2013).
555
556 **4.2 Comparison to Prior Work**
557 *4.2.1 Aging Induced Changes to Phyllomanganate Structures*
558 Previous research (Lanson et al., 2000; Manceau et al., 2013) has found that
559 phyllomanganate sheets undergo structural changes under acidic conditions in the absence of
560 Mn(II) that are consistent with those observed in the current study. High-energy X-ray scattering
561 and pair distribution function analysis demonstrates that structural Mn migrates into the
562 interlayers in δ-MnO_2 upon equilibration at low pH (Manceau et al., 2013). This results in
563 increased vacancy content and the formation of a supercell either through long range ordering of
564 sheet vacancies or ordering of interlayer Mn. In the current study, we also find that some layer
565 Mn is ejected from δ-MnO_2 sheets after aging at pH 4, but evidence of the formation of a
566 supercell only appears with the addition of Mn(II) to the δ-MnO_2 system. However, we do find
567 that a supercell may form in HexB aged at pH 4 in the absence of Mn(II), possibly because this
568 sample exceeds our hypothesized Mn(III) threshold for such restructuring. Previous research on
569 the structures of Na-birnessite [a triclinic birnessite (Post et al., 2002)] observed that the
570 phyllomanganate sheet transitioned towards hexagonal symmetry with increasing acidity (Drits

et al., 1997; Silvester et al., 1997; Lanson et al., 2000), consistent with our observation that TriB maintains its pseudo-orthogonal sheets after aging at pH 7 but forms hexagonal sheets at pH 4. One recent study, however, observed that TriB partially transforms to hexagonal H-birnessite at pH 7 in solutions containing 20 mM MES or HEPES buffers and in unbuffered solutions after 14 days (Ling et al., 2015). This distinct outcome compared to the present study and prior research (Drits et al., 1997; Silvester et al., 1997; Lanson et al., 2000) is of unclear origin. Substantial differences in the mineral to water ratio, concentration of buffers that may reduce manganese oxides (Elzinga and Kustka, 2015), and ionic strength among these experiments all may contribute to the contrasting observed stability of the triclinic birnessite structure.

4.2.2 Mn(II) Induced Changes to Phyllomanganate Structures

Although most studies of interactions between dissolved Mn(II) and solid manganese oxide in abiotic systems have largely focused on phase transformation behaviors (Elzinga, 2011; Lefkowitz et al., 2013; Elzinga and Kustka, 2015), some have indicated that Mn(II) can affect phyllomanganate sheet structures (Bargar et al., 2005; Zhu et al., 2010a; Lefkowitz et al., 2013), inducing changes similar to those observed in the present study. Previous research demonstrated that Mn(II) adsorbs above vacancies in a biogenic, hexagonally-symmetric manganese oxide but that interlayer Mn decreases with increasing pH, indicating that Mn(II) oxidizes via Mn(II)-Mn(IV) comproportionation and enters the phyllomanganate sheet as Mn(III) (Zhu et al., 2010a). The fraction of phyllomanganates with orthogonal structures was also found to increase with time during reaction of δ-MnO_2 with 100 μM dissolved Mn(II) at pH 8 (Bargar et al., 2005). Recent research also finds that under oxic conditions, δ-MnO_2 progressively transitions to a triclinic birnessite type structure upon aging with Mn(II) at pH ≥8, with increasing

transformations observed with increasing pH (Zhao et al., 2016). No structural transformations were observed at pH 7, consistent with the current study.

As in prior studies (Bargar et al., 2005; Elzinga, 2011; Lefkowitz et al., 2013), the addition of substantial Mn(II) to all mineral systems at pH 7 resulted in the precipitation of feitknechtite. These samples have measured AMOS values near 3.20 (Table 2) and XRD patterns indicative of a mixture of phases, dominated by feitknechtite. Our experiments were conducted with aqueous Mn(II) to solid Mn oxide ratios lower (3 mmol Mn(II) g^{-1}) than those previously required to precipitate feitknechtite at pH 7 under anoxic conditions (8 mmol Mn(II) g^{-1}, with no feitknechtite precipitation at 2-6 mmol Mn(II) g^{-1}) (Lefkowitz et al., 2013) and the solids in the present work have surface areas similar to or larger than those used in the previous studies. We hypothesize that the formation of feitknechtite at these lower Mn(II) contents is related to the longer reaction times in this current study (25 versus 8 days). We also observed minor feitknechtite precipitation at pH 7 with TriB at low initial Mn(II) concentrations (0.75 mM initial Mn(II); 0.3 mmol Mn(II) g^{-1}). This indicates that the initial structural Mn(III) content is an important factor in Mn(II)-induced phase transformations to MnOOH phases.

4.3 Relevance to Environmental and Geologic Systems

The results of this study suggest that phyllomanganates in natural systems interact with dissolved Mn(II) primarily through adsorption and comproportionation-disproportionation reactions, resulting in subtle alterations to phyllomanganate sheet structures. Although dissolved Mn(II) concentrations exhibit spatial and temporal variations in natural systems, these are often lower than those observed to induce phase transformations at circumneutral pH (Graybeal and Heath, 1984; Rajendran et al., 1992; Burdige, 1993; Van Cappellen et al., 1998; Tebo et al.,

617 2004; Tebo et al., 2005; Pakhomova et al., 2007). Thus, abiotic Mn(II)-phyllomanganate
618 interactions that occur in these systems likely involve Mn(II) adsorption and restructuring of
619 phyllomanganate sheets, depending on the pH of the system.
620 These Mn(II)-induced structural changes, as well as capping of vacancy sites, could cause
621 a reduction in overall reactivity of manganese oxides and in trace metal sorption. Because the
622 structural changes induced by aqueous Mn(II) results from a decreased Mn oxidation state in the
623 phyllomanganate sheet, Mn(II) uptake may change phyllomanganate reactivity towards redox-
624 active adsorbates. The adsorption of Mn(II) and subsequent restructuring of phyllomanganate
625 sheets observed at low pH suggests that Mn(II) may decrease trace metal sorption in acidic
626 systems by removing reactive sites. In environments at circumneutral to alkaline pH, such as
627 marine sediments and suboxic soils, the interaction of dissolved Mn(II) with trace metals on
628 phyllomanganate surfaces may be limited to competitive adsorption effects, such as capping
629 vacancies and thus decreasing the number of surface sites available for trace metal adsorption
630 (Toner et al., 2006; Peacock and Sherman, 2007; Manceau et al., 2007b; Peacock, 2009; Zhu et
631 al., 2010b) and later incorporation (Peacock and Sherman, 2007). However, natural waters have
632 more complex major cation compositions than the NaCl fluid studied here, and the effects of
633 fluid composition on Mn(II)-phyllomanganate interactions is unknown. Past work shows that
634 Ca^{2+} promotes structural transformations of phyllomanganate to pseudo-orthogonally symmetric
635 sheets (Webb et al., 2005b). It is thus possible that Ca^{2+} and other common cations in natural
636 waters may enhance Mn(II)-induced phyllomanganate structural changes and any associated
637 effects on trace metal binding. These implications are consistent with recent observations from a
638 cave system, where phyllomanganates formed in fluids with higher dissolved Mn(II)
639 concentrations have lower trace metal contents than those produced in low-Mn(II) settings

(Frierdich and Catalano, 2012). The results of the present study show that dissolved Mn(II) influences phyllomanganate sheet structures, potentially altering the sorption behavior and reactivities of these minerals in natural systems, and that environmental conditions such as pH and fluid composition are the dominant controls on Mn(II)-induced structural changes.

ACKNOWLEDGEMENTS

The National Science Foundation (NSF), Division of Earth Sciences, Geobiology and Low-Temperature Geochemistry Program supported this research through Grant No. EAR-1056480. Flynn was also supported by the NSF Graduate Research Fellowship program through Grant No. DGE-1143954. The facilities and instruments maintained by the Nano Research Facility at Washington University, supported by the NSF through Award No. ECS-0335765, were used to conduct ICP-OES analyses. XRD patterns were collected with the Bruker D8 Advance XRD instrument at Washington University in St. Louis, supported by the NSF through Award No. EAR-1161543. The pH 7 MES-buffer and pH 4 experiment XAFS spectra in this study were collected at the DuPont-Northwestern-Dow Collaborative Access Team (DND-CAT) located at Sector 5 of the Advanced Photon Source (APS). DND-CAT is supported by Northwestern University, E.I. DuPont de Nemours & Co., and The Dow Chemical Company. The pH 7 XAFS spectra were collected at APS beamline 12-BM-B. The APS is a U.S. Department of Energy (DOE) Office of Science User Facility operated for the DOE Office of Science by Argonne National Laboratory under Contract No. DE-AC02-06CH11357. The authors would particularly like to thank Qing Ma for his help in setting up and collecting XAFS spectra at 5-BM-D and Sungsik Lee and Benjamin Reinhart for their support of data collection at beamline 12-BM-B.

663

664 **ELECTRONIC ANNEX**

665 This document contains information regarding MES buffer effects at pH 7. In addition, figures of
666 XANES spectra of Mn oxidation state standards, EXAFS data and fits, XRD patterns of TriB
667 aged at pH 4, and XANES spectra and XRD patterns showing the impact of MES buffer on pH 7
668 samples are included. Data regarding spectral fitting results for EXAFS measurements,
669 diffraction lines of manganese (hydr)oxides, and Langmuir isotherm parameters for Mn(II)
670 adsorption experiments are also listed.

REFERENCES

Ankoudinov A. L. Relativistic Spin-dependent X-ray Absorption Theory, Ph.D. Thesis, University of Washington, 1996.

Bargar J. R., Fuller C. C., Marcus M. A., Brearley A. J., de la Rosa M. P., Webb S. M. and Caldwell W. A. (2009) Structural characterization of terrestrial microbial Mn oxides from Pinal Creek, AZ. *Geochim. Cosmochim. Acta* **73,** 889-910.

Bargar J. R., Tebo B. M., Bergmann U., Webb S. M., Glatzel P., Chiu V. Q. and Villalobos M. (2005) Biotic and abiotic products of Mn(II) oxidation by spores of the marine *Bacillus sp.* strain SG-1. *Am. Mineral.* **90,** 143-154.

Bargar J. R., Tebo B. M. and Villinski J. E. (2000) In situ characterization of Mn (II) oxidation by spores of the marine *Bacillus* sp. strain SG-1. *Geochim. Cosmochim. Acta* **64,** 2775-2778.

Brindley G. W. and Brown G. (1980) Crystal structures of clay minerals and their X-ray identification. *Mineralogical Society, London* 361-410.

Burdige D. J. (1993) The biogeochemistry of manganese and iron reduction in marine sediments. *Earth-Sci. Rev.* **35,** 249-284.

Canfield D. E., Thamdrup B. and Hansen J. W. (1993) The anaerobic degradation of organic matter in Danish coastal sediments: iron reduction, manganese reduction, and sulfate reduction. *Geochim. Cosmochim. Acta* **57,** 3867-3885.

Clement B. G., Luther III G. W. and Tebo B. M. (2009) Rapid, oxygen-dependent microbial Mn(II) oxidation kinetics at sub-micromolar oxygen concentrations in the Black Sea suboxic zone. *Geochim. Cosmochim. Acta* **73,** 1878-1889.

Dick G. J., Clement B. G., Webb S. M., Fodrie F. J., Bargar J. R. and Tebo B. M. (2009) Enzymatic microbial Mn(II) oxidation and Mn biooxide production in the Guaymas Basin deep-sea hydrothermal plume. *Geochim. Cosmochim. Acta* **73,** 6517-6530.

Drits V. A., Lanson B., Bougerol-Chaillout C., Gorshkov A. I. and Manceau A. (2002) Structure of heavy-metal sorbed birnessite: Part 2. Results from electron diffraction. *Am. Mineral.* **87,** 1646-1661.

Drits V. A., Lanson B. and Gaillot A. -C. (2007) Birnessite polytype systematics and identification by powder X-ray diffraction. *Am. Mineral.* **92,** 771-788.

Drits V. A., Lanson B., Gorshkov A. I. and Manceau A. (1998) Substructure and superstructure of four-layer Ca-exchanged birnessite. *Am. Mineral.* **83,** 97-118.

Drits V. A. and McCarty D. K. (1996) The nature of diffraction effects from illite and illite-smectite consisting of interstratified trans-vacant and cis-vacant 2:1 layers: A

semiquantitative technique for determination of layer-type content. *Am. Mineral.* **81,** 852-863.

Drits V. A., Silvester E., Gorshkov A. I. and Manceau A. (1997) Structure of synthetic monoclinic Na-rich birnessite and hexagonal birnessite: I. Results from X-ray diffraction and selected-area electron diffraction. *Am. Mineral.* **82,** 946-961.

Elzinga E. J. (2011) Reductive transformation of birnessite by aqueous Mn (II). *Environ. Sci. Technol.* **45,** 6366-6372.

Elzinga E. J. and Kustka A. B. (2015) A Mn-54 radiotracer study of Mn isotope solid-liquid exchange during reductive transformation of vernadite (δ-MnO2) by aqueous Mn (II). *Environ. Sci. Technol.* **49,** 4310-4316.

Emerson S., Kalhorn S., Jacobs L., Tebo B. M., Nealson K. H. and Rosson R. A. (1982) Environmental oxidation rate of manganese(II): bacterial catalysis. *Geochim. Cosmochim. Acta* **46,** 1073-1079.

Friedl G., Wehrli B. and Manceau A. (1997) Solid phases in the cycling of manganese in eutrophic lakes: New insights from EXAFS spectroscopy. *Geochim. Cosmochim. Acta* **61,** 275-290.

Frierdich A. J. and Catalano J. G. (2012) Distribution and speciation of trace elements in iron and manganese oxide cave deposits. *Geochim. Cosmochim. Acta* **91,** 240-253.

Golden D. C., Chen C. C. and Dixon J. B. (1987) Transformation of birnessite to buserite, todorokite, and manganite under mild hydrothermal treatment. *Clays Clay Miner.* **35,** 271-280.

Golden D. C., Dixon J. B. and Chen C. C. (1986) Ion exchange, thermal transformations, and oxidizing properties of birnessite. *Clays Clay Miner.* **34,** 511-520.

Grangeon S., Lanson B., Miyata N., Tani Y. and Manceau A. (2010) Structure of nanocrystalline phyllomanganates produced by freshwater fungi. *Am. Mineral.* **95,** 1608-1616.

Grangeon S., Manceau A., Guilhermet J., Gaillot A. C., Lanson M. and Lanson B. (2012) Zn sorption modifies dynamically the layer and interlayer structure of vernadite. *Geochim. Cosmochim. Acta* **85,** 302-313.

Graybeal A. L. and Heath G. R. (1984) Remobilization of transition metals in surficial pelagic sediments from the eastern Pacific. *Geochim. Cosmochim. Acta* **48,** 965-975.

Hinkle M. A. G., Wang Z., Giammar D. E. and Catalano J. G. (2015) Interaction of Fe(II) with phosphate and sulfate on iron oxide surfaces. *Geochim. Cosmochim. Acta* **158,** 130-146.

Krumbein W. E. and Jens K. (1981) Biogenic rock varnishes of the Negev Desert (Israel) and ecological study of iron and magnanese transformation by cyanobacteria and fungi. *Oceologia* **50,** 25-38.

Lanson B., Drits V. A., Gaillot A. -C., Silvester E., Plançon A. and Manceau A. (2002) Structure of heavy-metal sorbed birnessite: Part 1. Results from X-ray diffraction. *Am. Mineral.* **87,** 1631-1645.

Lanson B., Drits V. A., Silvester E. and Manceau A. (2000) Structure of H-exchanged hexagonal birnessite and its mechanism of formation from Na-rich monoclinic buserite at low pH. *Am. Mineral.* **85,** 826-838.

Lanson B., Marcus M. A., Fakra S., Panfili F., Geoffroy N. and Manceau A. (2008) Formation of Zn-Ca phyllomanganate nanoparticles in grass roots. *Geochim. Cosmochim. Acta* **72,** 2478-2490.

Lefkowitz J. P., Rouff A. A. and Elzinga E. J. (2013) Influence of pH on the reductive transformation of birnessite by aqueous Mn(II). *Environ. Sci. Technol.* **47,** 10364-10371.

Ling F. T., Heaney P. J., Post J. E. and Gao X. (2015) Transformations from triclinic to hexagonal birnessite at circumneutral pH induced through pH control by common biological buffers. *Chem. Geol.* **416,** 1-10.

Lopano C. L., Heaney P. J., Post J. E., Hanson J. and Komarneni S. (2007) Time-resolved structural analysis of K- and Ba-exchange reactions with synthetic Na-birnessite using synchrotron X-ray diffraction. *Am. Mineral.* **92,** 380-387.

Luther G. W. (2010) The role of one- and two-electron transfer reactions in forming thermodynamically unstable intermediates as barriers in multi-electron redox reactions. *Aquatic Geochemistry* **16,** 395-420.

Manceau A., Kersten M., Marcus M. A., Geoffroy N. and Granina L. (2007a) Ba and Ni speciation in a nodule of binary Mn oxide phase composition from Lake Baikal. *Geochim. Cosmochim. Acta* **71,** 1967-1981.

Manceau A., Lanson M. and Geoffroy N. (2007b) Natural speciation of Ni, Zn, Ba, and As in ferromanganese coatings on quartz using X-ray fluorescence, absorption, and diffraction. *Geochim. Cosmochim. Acta* **71,** 95-128.

Manceau A., Marcus M. A. and Grangeon S. (2012) Determination of Mn valence states in mixed-valent manganates by XANES spectroscopy. *Am. Mineral.* **97,** 816-827.

Manceau A., Marcus M. A., Grangeon S., Lanson M., Lanson B., Gaillot A. -C., Skanthakumar S. and Soderholm L. (2013) Short-range and long-range order of phyllomanganate nanoparticles determined using high-energy X-ray scattering. *J. Appl. Crystallogr.* **46,** 193-209.

Manceau A., Tommaseo C., Rihs S., Geoffroy N., Chateigner D., Schlegel M., Tisserand D., Marcus M. A., Tamura N. and Chen Z. -S. (2005) Natural speciation of Mn, Ni, and Zn at the micrometer scale in a clayey paddy soil using X-ray fluorescence, absorption, and diffraction. *Geochim. Cosmochim. Acta* **69,** 4007-4034.

Mandernack K. W., Post J. E. and Tebo B. M. (1995) Manganese mineral formation by bacterial spores of a marine *Bacillus*, strain SG-1: Evidence for the direct oxidation of Mn(II) to Mn(IV). *Geochim. Cosmochim. Acta* **59,** 4393-4408.

Marcus M. A., Manceau A. and Kersten M. (2004) Mn, Fe, Zn and As speciation in a fast-growing ferromanganese marine nodule. *Geochim. Cosmochim. Acta* **68,** 3125-3136.

McKenzie R. M. (1980) The adsorption of lead and other heavy metals on oxides of manganese and iron. *Soil Research* **18,** 61-73.

McKeown D. A. and Post J. E. (2001) Characterization of manganese oxide mineralogy in rock varnish and dendrites using X-ray absorption spectroscopy. *Am. Mineral.* **86,** 701-713.

Meldau R., Newesely H. and Strunz H. (1973) Zur Kristallchemie von Feitknechtit, β-MnOOH. *Naturwissenschaften* **60,** 387-387.

Morgan J. J. (2005) Kinetics of reaction between O_2 and Mn (II) species in aqueous solutions. *Geochim. Cosmochim. Acta* **69,** 35-48.

Morgan J. J. and Stumm W. (1964) Colloid-chemical properties of manganese dioxide. *J. Coll. Sci.* **19,** 347-359.

Murray J. W., Balistrieri L. S. and Paul B. (1984) The oxidation state of manganese in marine sediments and ferromanganese nodules. *Geochim. Cosmochim. Acta* **48,** 1237-1247.

Nealson K. H., Tebo B. M. and Rosson R. A. (1988) Occurrence and mechanisms of microbial oxidation of manganese. *Adv. Appl. Microbiol.* **33,** 2027-2035.

Nelson Y. M. and Lion L. W. (2003) Formation of biogenic manganese oxides and their influence on the scavenging of toxic trace elements. *Geochemical and Hydrological Reactivity of Heavy Metals in Soils. CRC Press* **200,** 169-186.

Newville M. (2001) IFEFFIT: interactive EXAFS analysis and FEFF fitting. *J. Synchrotron Radiat.* **8,** 322-324.

Pakhomova S. V., Hall P. O., Kononets M. Y., Rozanov A. G., Tengberg A. and Vershinin A. V. (2007) Fluxes of iron and manganese across the sediment--water interface under various redox conditions. *Mar. Chem.* **107,** 319-331.

Peacock C. L. (2009) Physiochemical controls on the crystal-chemistry of Ni in birnessite: Genetic implications for ferromanganese precipitates. *Geochim. Cosmochim. Acta* **73,** 3568-3578.

Peacock C. L. and Sherman D. M. (2007) Crystal-chemistry of Ni in marine ferromanganese crusts and nodules. *Am. Mineral.* **92,** 1087-1092.

Post J. E. (1999) Manganese oxide minerals: Crystal structures and economic and environmental significance. *Proc. Natl. Acad. Sci. U. S. A.* **96,** 3447-3454.

Post J. E. and Appleman D. E. (1988) Chalcophanite, $ZnMn_3O_7$-$3H_2O$: New crystal-structure determinations. *Am. Mineral.* **73,** 1401-1404.

Post J. E., Heaney P. J. and Hanson J. (2002) Rietveld refinement of a triclinic structure for synthetic Na-birnessite using synchrotron powder diffraction data. *Powder Diffr.* **17,** 218-221.

Post J. E. and Veblen D. R. (1990) Crystal structure determinations of synthetic sodium, magnesium, and potassium birnessite using TEM and the Rietveld method. *Am. Mineral.* **75,** 477-489.

Post J. E., Von Dreele R. B. and Buseck P. R. (1982) Symmetry and cation displacements in hollandites: structure refinements of hollandite, cryptomelane and priderite. *Acta Crystallogr., Sect. B: Struct. Sci.* **38,** 1056-1065.

Rajendran A., Kumar M. D. and Bakker J. F. (1992) Control of manganese and iron in Skagerrak sediments (northeastern North Sea). *Chem. Geol.* **98,** 111-129.

Ravel B. and Newville M. (2005) ATHENA, ARTEMIS, HEPHAESTUS: data analysis for X-ray absorption spectroscopy using IFEFFIT. *J. Synchrotron Radiat.* **12,** 537-541.

Santelli C. M., Webb S. M., Dohnalkova A. C. and Hansel C. M. (2011) Diversity of Mn oxides produced by Mn(II)-oxidizing fungi. *Geochim. Cosmochim. Acta* **75,** 2762-2776.

Saratovsky I., Wightman P. G., Pasten P. A., Gaillard J. F. and Poeppelmeier K. R. (2006) Manganese oxides: Parallels between abiotic and biotic structures. *J. Am. Chem. Soc.* **128,** 11188-11198.

Shimmield G. B. and Price N. B. (1986) The behaviour of molybdenum and manganese during early sediment diagenesis off shore Baja California, Mexico. *Mar. Chem.* **19,** 261-280.

Silvester E., Manceau M. and Drits V. A. (1997) Structure of synthetic monoclinic Na-rich birnessite and hexagonal birnessite: II. Results from chemical studies and EXAFS spectroscopy. *Am. Mineral.* **82,** 962-978.

Tan H., Zhang G., Heaney P. J., Webb S. M. and Burgos W. D. (2010) Characterization of manganese oxide precipitates from Appalachian coal mine drainage treatment systems. *Appl. Geochem.* **25,** 389-399.

Tebo B. M. (1991) Manganese (II) oxidation in the suboxic zone of the Black Sea. *Deep-Sea Res* **38,** S883-S905.

Tebo B. M., Bargar J. R., Clement B. G., Dick G. J., Murray K. J., Parker D., Verity R. and Webb S. M. (2004) Biogenic manganese oxides: Properties and mechanisms of formation. *Annu. Rev. Earth Pl. Sc.* **32,** 287-328.

Tebo B. M., Ghiorse W. C., van Waasbergen L. G., Siering P. L. and Caspi R. (1997) Bacterially mediated mineral formation; insights into manganese (II) oxidation from molecular genetic and biochemical studies. *Rev. Mineral. Geochem.* **35,** 225-266.

Tebo B. M., Johnson H. A., McCarthy J. K. and Templeton A. S. (2005) Geomicrobiology of manganese(II) oxidation. *Trends Microbiol.* **13,** 421-428.

Toner B., Manceau A., Webb S. M. and Sposito G. (2006) Zinc sorption by biogenic hexagonal birnessite particles within a hydrated bacterial biofilm. *Geochim. Cosmochim. Acta* **70,** .

Tu S., Racz G. J. and Goh T. B. (1994) Transformations of synthetic birnessite as affected by pH and manganese concentration. *Clays Clay Miner.* **42,** 321-330.

Van Cappellen P., Viollier E., Roychoudhury A., Clark L., Ingall E., Lowe K. and Dichristina T. (1998) Biogeochemical cycles of manganese and iron at the oxic-anoxic transition of a stratified marine basin (Orca Basin, Gulf of Mexico). *Environ. Sci. Technol.* **32,** 2931-2939.

Viani A., Gualtieri A. F. and Artioli G. (2002) The nature of disorder in montmorillonite by simulation of X-ray powder patterns. *Am. Mineral.* **87,** 966-975.

Villalobos M., Lanson B., Manceau A., Toner B. and Sposito G. (2006) Structural model for the biogenic Mn oxide produced by *Pseudomonas putida*. *Am. Mineral.* **91,** 489-502.

Villalobos M., Toner B., Bargar J. R. and Sposito G. (2003) Characterization of the manganese oxide produced by *pseudomonas putida* strain MnB1. *Geochim. Cosmochim. Acta* **67,** 2649-2662.

Von Langen P. J., Johnson K. S., Coale K. H. and Elrod V. A. (1997) Oxidation kinetics of manganese (II) in seawater at nanomolar concentrations. *Geochim. Cosmochim. Acta* **61,** 4945-4954.

Webb S. M. (2005) SIXPack: A Graphical User Interface for XAS Analysis using IFEFFIT. *Phys. Scripta* **T115,** 1011-1014.

Webb S. M., Tebo B. M. and Bargar J. R. (2005a) Structural characterization of biogenic Mn oxides produced in seawater by the marine *bacillus sp.* strain SG-1. *Am. Mineral.* **90,** 1342-1357.

Webb S. M., Tebo B. M. and Bargar J. R. (2005b) Structural influences of sodium and calcium ions on the biogenic manganese oxides produced by the marine *Bacillus sp.*, strain SG-1. *Geomicrobiol. J.* **22,** 181-193.

Wehrli B., Friedl G. and Manceau A. Reaction rates and products of manganese oxidation at the sediment-water interface, In *Advances in Chemistry,* 1995; pp. 111-134.

Yu Q., Sasaki K., Tanaka K., Ohnuki T. and Hirajima T. (2012) Structural factors of biogenic birnessite produced by fungus *Paraconiothyrium* sp. WL-2 strain affecting sorption of Co^{2+}. *Chem. Geol.* **310-311,** 106-113.

Zhao H., Zhu M., Li W., Elzinga E. J., Villalobos M., Liu F., Zhang J., Feng X. and Sparks D. L. (2016) Redox reactions between Mn(II) and hexagonal birnessite change its layer symmetry. *Environ. Sci. Technol.* **50,** 1750-8.

Zhu M., Ginder-Vogel M., Parikh S. J., Feng X. H. and Sparks D. L. (2010a) Cation effects on the layer structure of biogenic Mn-oxides. *Environ. Sci. Technol.* **44,** 4465-4471.

Zhu M., Ginder-Vogel M. and Sparks D. L. (2010b) Ni(II) sorption on biogenic Mn-oxides with varying Mn octahedral layer structure. *Environ. Sci. Technol.* **44,** 4472-4478.

Table 1. Structural Mn and Na content and relative amounts of initial dissolved Mn^{2+} and solid Mn^{4+} in the 25 day aging experiments.

Mineral	Moles $Mn_{(s)}$ per g mineral	Moles Na per g mineral	Na:Mn (mol:mol)	Initial $Mn^{2+}_{(aq)}$:$Mn^{4+}_{(s)}$ (mol:mol) 0.75 mM Mn(II)	Initial $Mn^{2+}_{(aq)}$:$Mn^{4+}_{(s)}$ (mol:mol) 7.5 mM Mn(II)
δ-MnO₂	0.0067	0.0011	0.16	0.045	0.450
HexB	0.0083	0.0002	0.02	0.042	0.452
TriB	0.0097	0.0027	0.28	0.054	0.543

Table 2. Properties of synthesized and reacted phyllomanganates, including the reaction conditions and final solution concentrations for the aging experiments.

Sample ID	Mn Oxide	pH	$[Mn(II)]_{initial}$ (mM)	XANES AMOS[a]	MB AMOS[b]	$[Mn]_{soln}$ (mM)	$[Mn]_{ads}$ (mmol g^{-1})
Unreacted:							
Synthδ	δ-MnO_2			3.99			
SynthHB	HexB			3.80			
SynthTB	TriB			3.57			
Aging Samples:							
4δno	δ-MnO_2	4	0	3.93	3.99	0.012 ± 0.001	-0.005[c]
4δlow	δ-MnO_2	4	0.75	3.82	3.91	BDL[d]	0.30
4δhigh	δ-MnO_2	4	7.5	3.67	3.68	4.4 ± 0.1	1.24
7δno	δ-MnO_2	7	0	3.98	3.99	BDL	-
7δlow	δ-MnO_2	7	0.75	3.94	3.91	BDL	0.30
7δhigh	δ-MnO_2	7	7.5	3.22	3.38	BDL	3.00
4HexBno	HexB	4	0	3.79	3.80	BDL	-
4HexBlow	HexB	4	0.75	3.64	3.77	0.48 ± 0.02	0.11
4HexBhigh	HexB	4	7.5	--[e]	3.73	6.8 ± 0.2	0.28
7HexBno	HexB	7	0	3.79	3.80	BDL	-
7HexBlow	HexB	7	0.75	3.72	3.73	BDL	0.30
7HexBhigh	HexB	7	7.5	3.21	3.27	BDL	3.00
4TriBno	TriB	4	0	3.67	3.61	0.43 ± 0.01	-0.17
4TriBlow	TriB	4	0.75	3.63	3.63	0.88 ± 0.03	-0.05
4TBhigh	TriB	4	7.5	3.60	3.60	6.70 ± 0.08	0.32
7TriBno	TriB	7	0	3.60	3.57	BDL	-
7TriBlow	TriB	7	0.75	3.53	3.51	BDL	0.30
7TriBhigh	TriB	7	7.5	3.11	3.10	BDL	3.00

[a] Average manganese oxidation state (AMOS) determined by XANES. Estimated accuracy is approximately 0.04 v.u. (Manceau et al., 2012)

[b] AMOS predicted by mass balance (MB).

[c] Negative value indicates net release of Mn(II) to solution.

[d] BDL denotes below detection limit (0.006 mM).

[e] No XANES data is presented for this sample because it was damaged prior to analysis.

FIGURE CAPTIONS

Figure 1. XRD patterns of unreacted manganese oxides (A) and of δ-MnO2 (B), HexB (C), and TriB (D) after aging for 25 days in the absence or presence of dissolved Mn(II); see Table 2 for specific conditions. In (B-D), patterns of the unreacted samples (black) and samples reacted without Mn(II) (see legend) are overplotted by the pattern of the corresponding sample reacted with Mn(II) (see legend). The red asterisk in (D) denotes a peak corresponding to feitknechtite. The vertical dashed line in (D) demarcates an intensity scale change from 1× to 8× intensity.

Figure 2. Mn K-edge XAFS spectra of unreacted and reacted δ-MnO_2 (A-C), HexB (D-F), and TriB (G-I); see Table 2 for specific conditions. XANES spectra (A,D,G), EXAFS spectra (B,E,H), or Fourier transform (C,F,I) data of the aged samples are overplotted with one another for each pH set. Vertical blue lines denote diagnostic features at 6553 eV in the XANES spectra, 6.8, 8.1, and 9.2 $Å^{-1}$ in the EXAFS spectrum, and 3.0 and 5.2 Å in the EXAFS Fourier transform; the vertical black dashed line indicates the white line energy of unreacted triclinic birnessite. XAFS spectra of samples reacted with 7.5 mM Mn(II) at pH 7 appear in Figure 4.

Figure 3. (A) Mn(II) adsorption isotherms at pH 4 after 2 days of reaction. Lines represent Langmuir isotherm fits to the data (see Table EA1). (B) Mn(II) uptake (points) onto phyllomanganates after 25 days of reaction at pH 4 compared to Langmuir isotherm curves determined from the 2 day Mn(II) adsorption isotherm measurements.

Figure 4. XRD patterns (A) and XANES spectra (B) of phyllomanganates reacted for 25 days with 7.5 mM Mn(II). Peaks corresponding to feitknechtite in XRD are denoted by red asterisks. Dotted lines represent XANES spectra of the corresponding unreacted phyllomanganate.

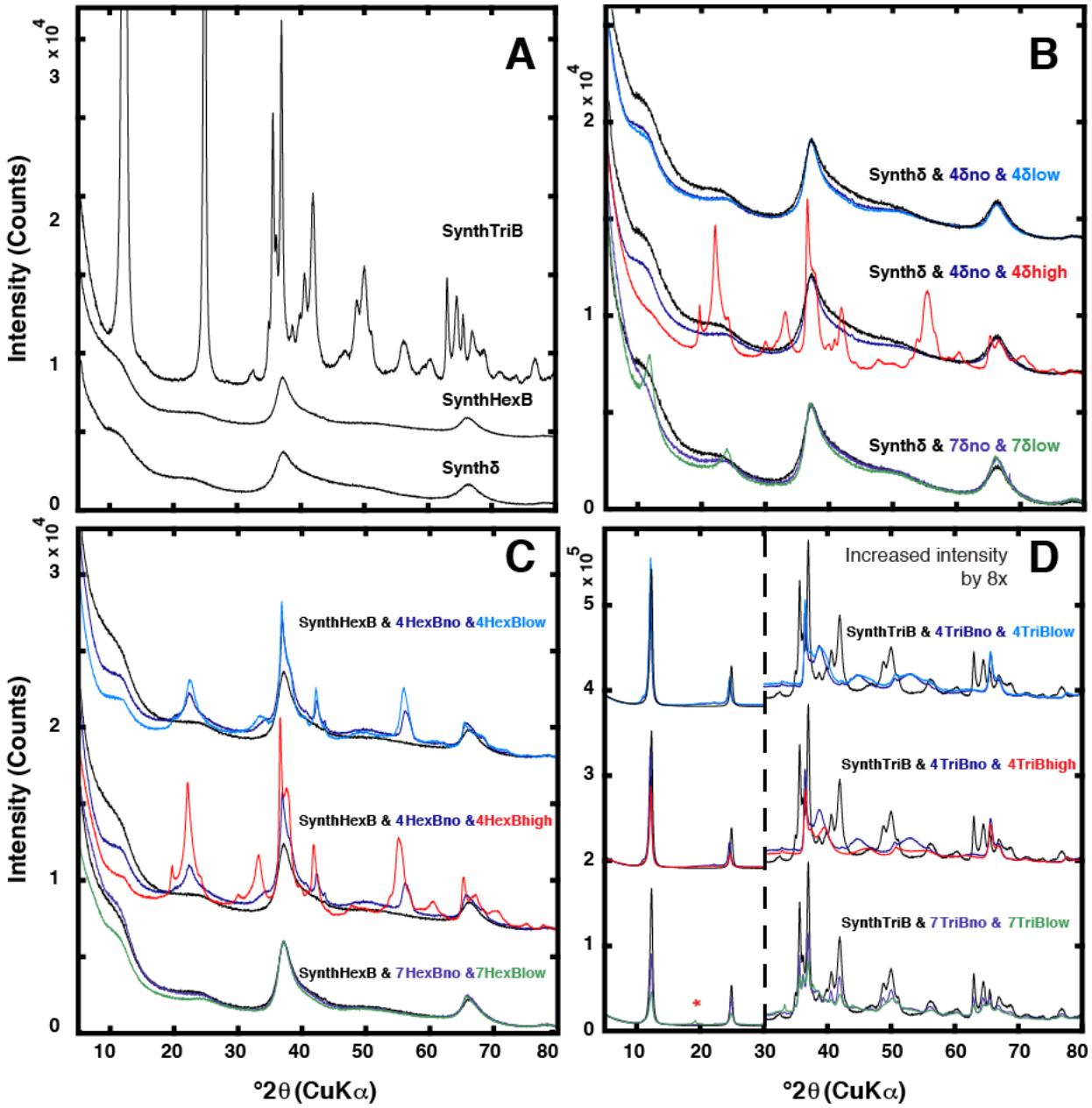

Figure 1. XRD patterns of unreacted manganese oxides (A) and of δ-MnO2 (B), HexB (C), and TriB (D) after aging for 25 days in the absence or presence of dissolved Mn(II); see Table 2 for specific conditions. In (B-D), patterns of the unreacted samples (black) and samples reacted without Mn(II) (see legend) are overplotted by the pattern of the corresponding sample reacted with Mn(II) (see legend). The red asterisk in (D) denotes a peak corresponding to feitknechtite. The vertical dashed line in (D) demarcates an intensity scale change from 1× to 8× intensity.

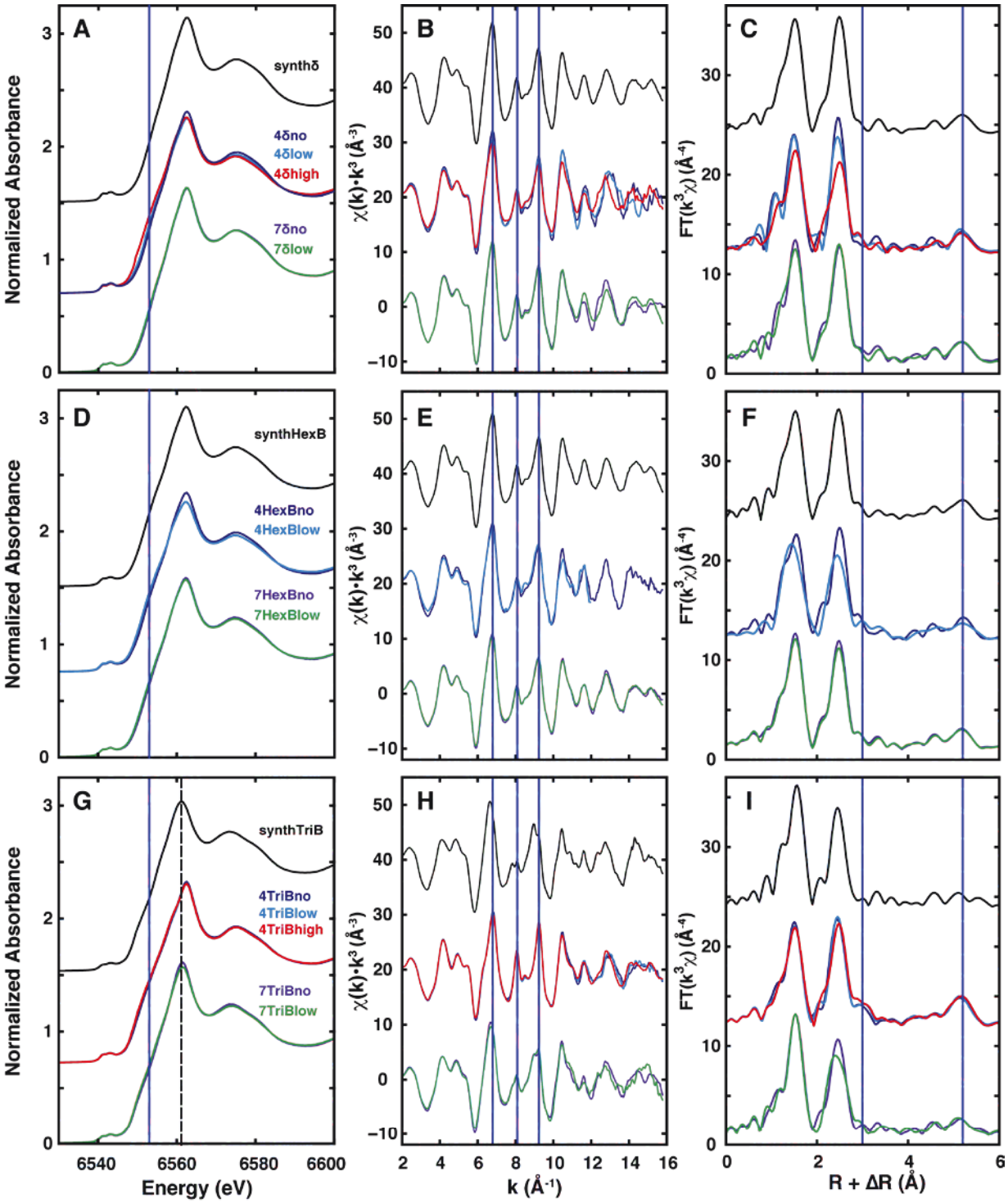

Figure 2. Mn K-edge XAFS spectra of unreacted and reacted δ-MnO_2 (A-C), HexB (D-F), and TriB (G-I); see Table 2 for specific conditions. XANES spectra (A,D,G), EXAFS spectra (B,E,H), or Fourier transform (C,F,I) data of the aged samples are overplotted with one another for each pH set. Vertical blue lines denote diagnostic features at 6553 eV in the XANES spectra, 6.8, 8.1, and 9.2 $Å^{-1}$ in the EXAFS spectrum, and 3.0 and 5.2 Å in the EXAFS Fourier transform; the vertical black dashed line indicates the white line energy of unreacted triclinic birnessite. XAFS spectra of samples reacted with 7.5 mM Mn(II) at pH 7 appear in Figure 4.

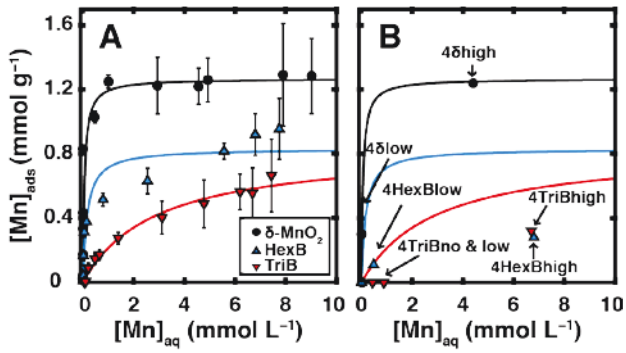

Figure 3. (A) Mn(II) adsorption isotherms at pH 4 after 2 days of reaction. Lines represent Langmuir isotherm fits to the data (see Table EA1). (B) Mn(II) uptake (points) onto phyllomanganates after 25 days of reaction at pH 4 compared to Langmuir isotherm curves determined from the 2 day Mn(II) adsorption isotherm measurements.

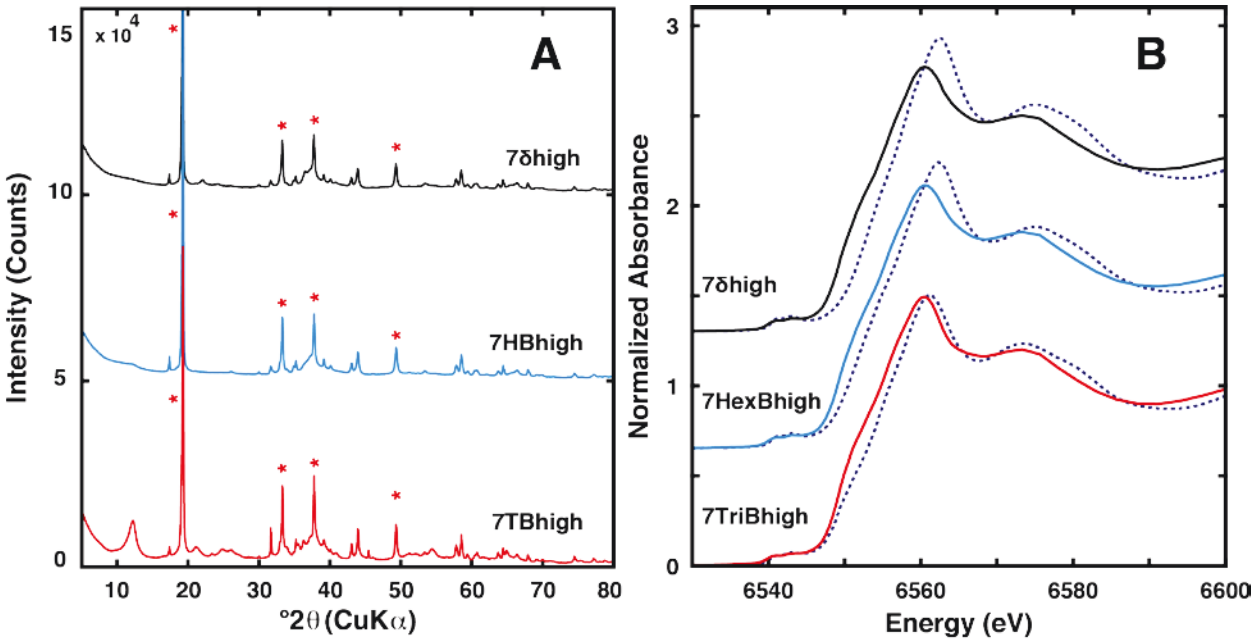

Figure 4. XRD patterns (A) and XANES spectra (B) of phyllomanganates reacted for 25 days with 7.5 mM Mn(II). Peaks corresponding to feitknechtite in XRD are denoted by red asterisks. Dotted lines represent XANES spectra of the corresponding unreacted phyllomanganate.